

A Wearable Attitude-Measurement System Using a Fiberoptic Gyroscope

Abstract

An attitude-measurement system (TISS-5-40) has been developed to achieve a wearable sensor for individuals. This equipment is one of the inertial sensor systems having three fiberoptic gyroscopes and three accelerometers. Heading stability of 1 deg./hr. (1σ) and attitude accuracy of ± 0.5 deg. have been demonstrated. At present, some of the attitude-measurement Systems have been applied in the field of mixed-reality technology, and the users confirm and report its effectiveness (Hara, Anabuki, Satoh, Yamamoto, & Tamura, 2000).

1 Introduction

In the field of mixed-reality technology, one of the image-positioning methods that are suitable for computer graphics images on real image basis is a tracker-based method (Tamura & Ohta, 1998). This technique requires a high-accuracy attitude-measurement system for wearable applications. Systems using magnetic (Ohshima, Satoh, Yamamoto, & Tamura, 1999) and inertial sensors aided by ultrasonic rangefinders (Foxlin, Harrington, & Pfeifer, 1998) have been used for human-motion attitude measurement. These systems, however, are not good for desirable outdoor use because of their limited measurable range.

Recent development in inertial sensor technology makes the attitude-measurement system possible for such outdoor applications. Although various kinds of inertial sensor systems are available, wearable attitude-measurement systems with vibratory gyroscopes (widely used in automobile navigation) in combination with a compass and a tilt-orientation sensor have been publicized for outdoor applications (Azuma, Hoff, Neely, & Sarfaty, 1999).

On the other hand, there is a trend away from conventional mechanical gyroscope systems that employ a spinning mass toward fiberoptic gyroscopes (FOG) to achieve high-accuracy attitude-measurement systems for aircraft and ships. An attitude-measurement system with high accuracy and minimal size is made possible by cutting-edge technologies in electronics, optics, and micro-manufacturing.

This report outlines our work on the fiberoptic gyroscope-based wearable attitude-measurement system, which demonstrates its sufficient attitudinal accuracy.



Figure 1. Outer view of the sensor.

2 Wearable Attitude-Measurement System

Our recently developed wearable attitude-measurement system can be worn on the head of an individual to measure his or her attitude (heading, pitch, and roll). To measure one's attitude without any external information, it is necessary to get three-axes data of rotation rate and acceleration orthogonally crossing each other. The rotation rate and an acceleration are measured by a gyroscope and an accelerometer, respectively.

Figure 1 shows the outer view of the attitude measurement system sensor, and figure 2 shows the sensor's inside structure. To avoid hindering or impeding head movement because of increased inertial moment with the head-mounted sensor, the sensor is designed to be

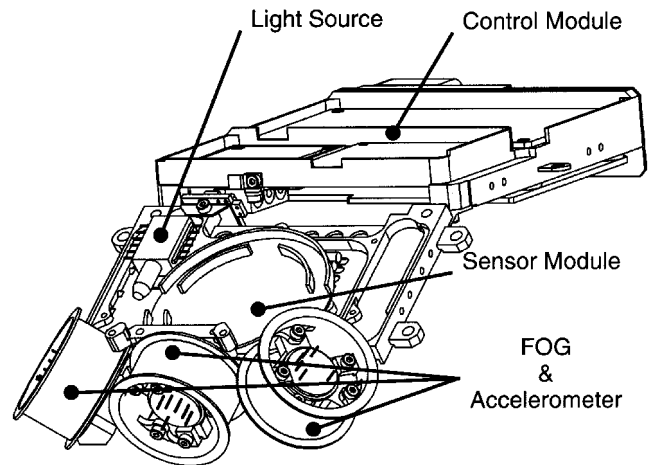


Figure 2. Inside structure of the sensor.

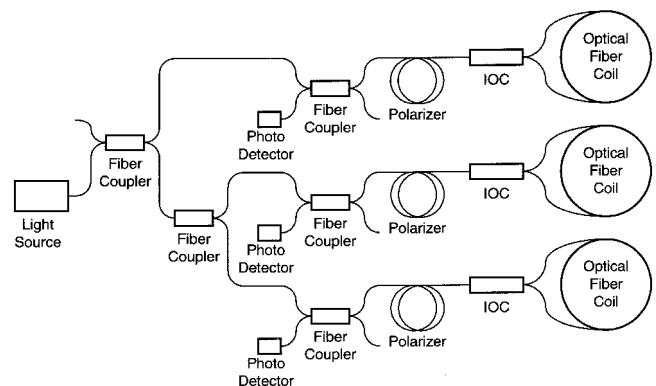


Figure 3. Optical configuration.

as thin and light as possible. The sensor unit consists of a sensor module and a control module. The sensor module has three FOG axes and three accelerometer axes that input axes cross-orthogonally to each other. The control module is composed of a light source control, a photo detector, a FOG control, and CPU circuits.

To achieve the smaller size, the sensor adopts a configuration in which a single light source drives three FOG axes as shown in figure 3, eliminating two light sources and their control circuits. Each FOG axis consists of a fiber coupler, a polarizer, and an integrated optic circuit (IOC) with phase modulator and sensing

Table 1. *Sensor Specifications*

Parameters	Specifications		
Model name	TISS-50-40	InterTrax 30	3DM
Manufacturer	Tokimec	InterSence	MicroStrain
Sensor type	FOG	Vibratory Gyro	Magnetic sensor
Heading accuracy	1 deg./hr. (1σ)	—	± 1.0 deg.
Attitude accuracy	± 0.5 deg.	—	Pitch: ± 0.93 deg. Roll: ± 0.33 deg.
Scale factor accuracy	Heading: $\pm 0.1\%$	—	$\pm 0.23\%$ F.S.
Input rotation rate	458 deg./sec. (maximum)	Yaw:400 deg./sec. Pitch, Roll:360 deg./sec.	—
Input acceleration	78 m./sec. ² (maximum)	—	—
Range of attitude			
Heading	± 180 deg.	± 180 deg.	± 180 deg.
Pitch	± 90 deg.	± 90 deg.	± 180 deg.
Roll	± 180 deg.	± 180 deg.	± 70 deg.
Alignment time	1 min.	—	—
Alignment accuracy	± 0.5 deg.	—	—
Dimensions	$121 \times 107 \times 43$ mm ³ (Sensor module) $100 \times 122 \times 26$ mm ³ (Control module)	$81 \times 46 \times 58$ mm ³	$52 \times 97 \times 23$ mm ³
Weight	550 g (maximum)	145 g	—
Power supply	+5 V, 2 A +12 V, 0.3 A −12 V, 0.3 A	DC 9 V	DC 5.3 V to 12 V
Protocol	RS232	RS232	RS323 or RS485
Update frequency	250 Hz	256 Hz	30 Hz
Latency	2 ms	38 ms \pm 2 ms	—

(—) represents no nominal value.

coil. Sensor specifications are shown in table 1 with the ones of other sensors used for comparison in figure 14.

3 Measurement System Components

3.1 Fiberoptic Gyroscope

The fiberoptic gyroscope (FOG) sensor detects the Sagnac effect using a ring interferometer (Ezekiel &

Arditty, 1982; Lefevre, 1993). The Sagnac effect is a phenomenon that causes a difference in optical paths between two optical waves propagating in opposite directions in a closed optical path rotating in inertial space. This difference in optical paths can be expressed as a difference in optical phase, the *Sagnac phase shift* (ϕ_s). This phase shift is given in equation (1):

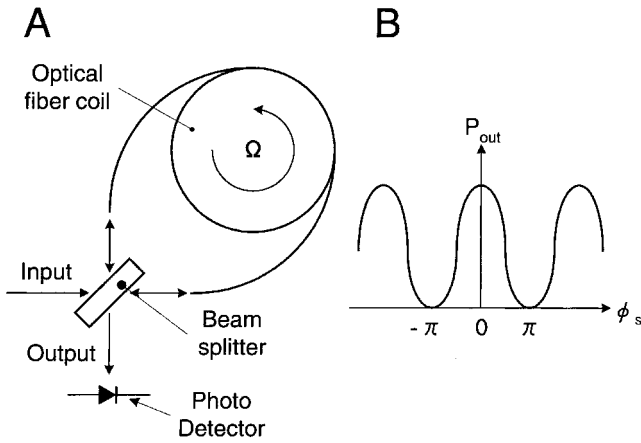


Figure 4. Basic FOG.

$$\phi_s = \frac{2\pi LD}{\lambda c} \times \Omega, \quad (1)$$

where L is the length of the optical path, D is its diameter, λ is the wave length of light, c is the velocity of light in free space, and Ω is the rotation rate. The basic FOG is shown in figure 4(A). Input light from a light source is divided into two optical waves (50/50) at the beam splitter and are launched in opposite directions along the coil of optical fiber. The two waves propagated around through the coil interfere at the beam splitter. The power of the interfered light is given in equation (2) as a function of the Sagnac phase shift ϕ_s :

$$P_{out} = \frac{P_{in}}{2} (1 + \cos \phi_s) \quad (2)$$

The relation between the Sagnac phase shift (that is, the rotation rate) and the power of interfered light is shown in figure 4(B). Because of insensitivity near a rotation rate of zero, the sensitivity is improved by phase modulation of the optical wave propagating through the fiber coil and synchronous demodulation of the detected optical signal at the photo detector (Ulrich, 1980). The optical signal modulated with a sinusoidal signal of frequency f_m given in equation (3) is represented in equation (4) and expanded to equation (5):

$$\Delta \phi_m(t) = \phi_b \cos(2\pi f_m t) \quad (3)$$

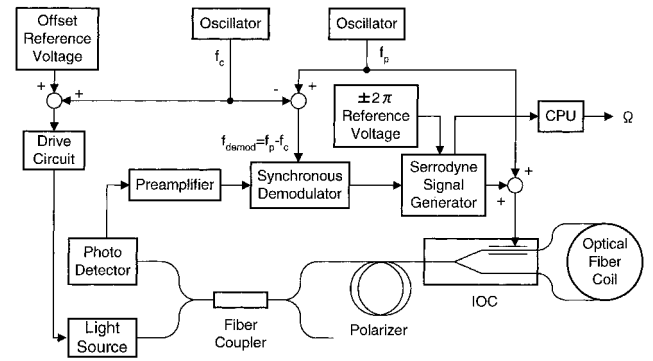


Figure 5. Block diagram of optical superheterodyne.

$$P_{out} = \frac{P_{in}}{2} [1 + \cos\{\phi_s + \phi_b \cos(2\pi f_m t)\}] \quad (4)$$

$$P_{out} = \frac{P_{in}}{2} [1 + \cos \phi_s \cos\{\phi_b \cos(2\pi f_m t)\} - \sin \phi_s \sin\{\phi_b \cos(2\pi f_m t)\}] \quad (5)$$

To expand equation (5) using the Bessel function of the first kind, the output signal is obtained as equation (6):

$$P_{out} = \frac{P_{in}}{2} \times \left[1 + \cos \phi_s \{J_0(\phi_b) + 2J_2(\phi_b) \cos(4\pi f_m t) + \dots\} + \sin \phi_s \{2J_1(\phi_b) \sin(2\pi f_m t) + 2J_3(\phi_b) \sin(6\pi f_m t) + \dots\} \right] \quad (6)$$

The output signal shown in equation (6) to be applied to the synchronous demodulation at the frequency f_m is given in equation (7):

$$P_{demod} = P_{in} J_1(\phi_b) \sin \phi_s \quad (7)$$

Because this equation is given as a sine function of ϕ_s , the sensitivity of near-zero rotation is improved. In addition, to expand the dynamic range and to improve the linearity of the scale factor, closed-loop operation is used. Figure 5 shows a block diagram of the recently developed FOG. The size of the FOG control circuit is minimized by adopting the optical superheterodyne method (which modulates the light source), in addition to phase modulation and closed-loop operation.

3.2 Accelerometer

This sensor system uses a crystal resonating accelerometer (Honeywell RBA-500) to minimize the size of the overall system. This accelerometer detects frequency variations in the crystal oscillator in response to input acceleration, and its output is essentially digital (frequency). Because of the digital output, the interface circuit connection with the calculating circuit can be eliminated to reduce size.

4 Inertial Calculation

In inertial calculation, alignment determines the initial attitude of the sensor system, and successive attitude calculations update the sensor attitude. The attitude is defined by the coordinate system (shown in figure 6). The $0-X_L Y_L Z_L$ frame is called the *local frame*, being fixed on the earth surface and its $X_L Y_L$ plane is parallel to the horizontal plane and its X_L axis points towards the north. The $0-X_B Y_B Z_B$ frame is also called the *body frame*, being fixed on the object plane to measure its own attitude. Angles ϕ , θ , and ψ represent heading, pitch, and roll, respectively, and are called *Euler's angles*. Using the three angles, the relationship between $0-X_L Y_L Z_L$ and $0-X_B Y_B Z_B$ is given in equation (8).

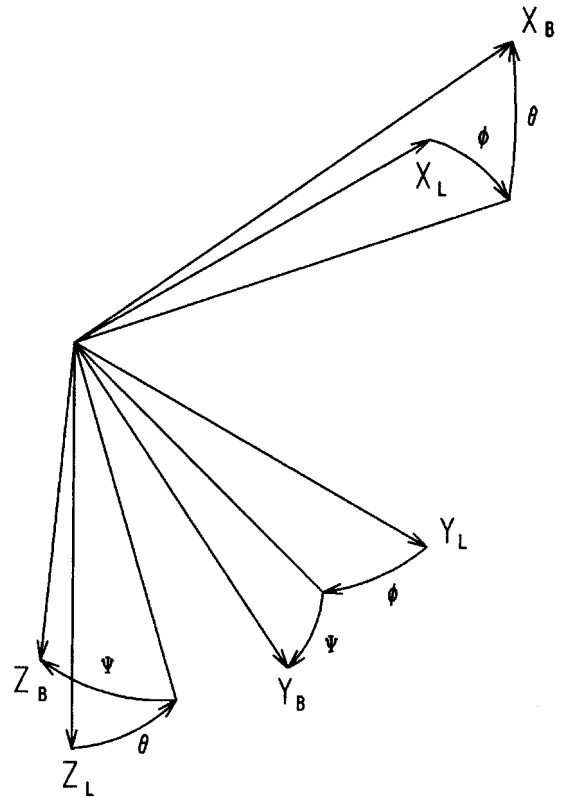


Figure 6. Coordinate system.

$$\begin{bmatrix} V_{XB} \\ V_{YB} \\ V_{ZB} \end{bmatrix} = \begin{bmatrix} \cos \phi \cdot \cos \theta & \sin \phi \cdot \cos \theta & -\sin \theta \\ -\sin \phi \cdot \cos \psi + \cos \phi \cdot \sin \theta \cdot \sin \psi & \cos \phi \cdot \cos \psi + \sin \phi \cdot \sin \theta \cdot \sin \psi & \cos \theta \cdot \sin \psi \\ \sin \phi \cdot \sin \psi + \cos \phi \cdot \sin \theta \cdot \cos \psi & -\cos \phi \cdot \sin \psi + \sin \phi \cdot \sin \theta \cdot \cos \psi & \cos \theta \cdot \cos \psi \end{bmatrix} \begin{bmatrix} V_{XL} \\ V_{YL} \\ V_{ZL} \end{bmatrix} \quad (8)$$

4.1 Alignment

Initial attitude of the sensor (ϕ_0 , θ_0 , and ψ_0) is determined as follows. Initial heading ($\phi_0 = 0$) can be obtained to set the x axis of the sensor toward north. Initial pitch (θ_0) and roll (ψ_0) can be obtained to solve equation (8) for θ , ψ by substituting in equation (9) and (10).

$$[0 \ 0 \ -g] = [V_{XL} \ V_{YL} \ V_{ZL}] \quad (9)$$

$$[A_{XB} \ A_{YB} \ A_{ZB}] = [V_{XB} \ V_{YB} \ V_{ZB}] \quad (10)$$

Equation (9) represents gravitational acceleration on the local frame, and equation (10) represents the component of gravitational acceleration on the body frame, which is detected by three accelerometers.

4.2 Attitude Calculation

Inertial calculation has two methods: the strap-down and the platform method. The strap-down method is just to fix the gyroscopes and accelerometers

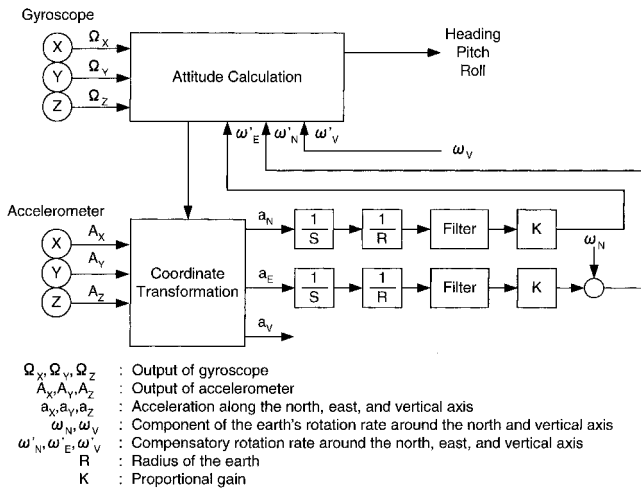


Figure 7. Block diagram of attitude calculation.

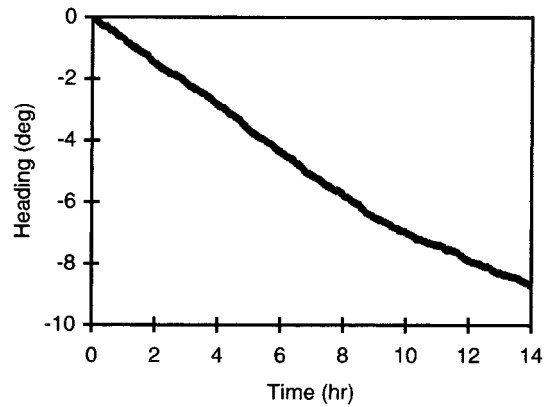


Figure 8. Drift of heading.

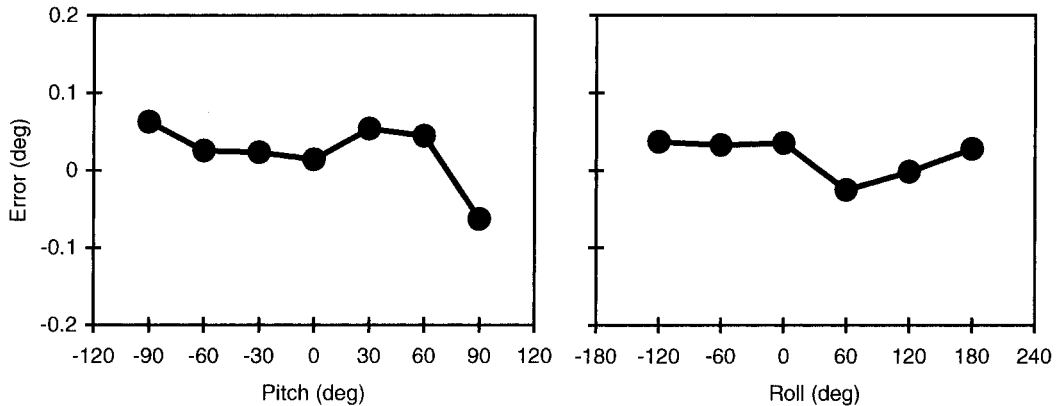


Figure 9. Accuracy of attitude.

directly to the body. Contrastingly, the platform method requires the gyroscopes and accelerometers to be fixed on the stabilized platform that employs the gimbal mechanism. With the platform method, the attitude is achieved by the relative angle among gimbals on the platform being precisely supported its attitude horizontally in north-seeking operation with the signals from each sensor. It is clear that the strap-down method enables smaller sensors for the new sensor system. However, the method requires that the gyros have a wide dynamic range and high resolution because rotation of the body is detected directly. The FOG sensor satisfies

the requirement. To reduce calculation error, it is necessary to shorten the attitude-calculation cycle as much as possible, and this requires a high-speed CPU. To achieve high-speed calculation, this sensor adopted the Hitachi SH-4 for the CPU.

Figure 7 shows the block diagram of the attitude calculation. The four-parameter method (quaternion method) is used for the attitude calculation and the transformation between coordinates because it excels in calculation speed. McKern (1968) described the transformation that employs the quaternion in a strap-down inertial guidance system. An outline of attitude calcula-



Figure 10. The three-axes rate table that was employed to evaluate for the accuracy of the attitude.

tion using the quaternion is shown as follows: The quaternion has a scalar part and a three dimensional vector part (given in equation (11))

$$q = \lambda + i\vec{\rho}_x + j\vec{\rho}_y + k\vec{\rho}_z, \quad (11)$$

and its conjugate is given in equation (12):

$$q' = \lambda - (i\vec{\rho}_x + j\vec{\rho}_y + k\vec{\rho}_z) \quad (12)$$

Then, the transformation from body frame to local frame is represented as in equation (13) using these two quaternions,

$$\vec{V}^L = q\vec{V}^Bq' \quad (13)$$

and the norm of the quaternion must be satisfied in equation (14):

$$N(q) = 1 \quad (14)$$

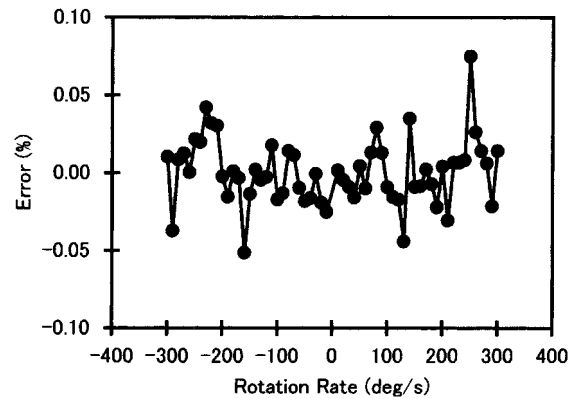


Figure 11. Accuracy of scale factor.

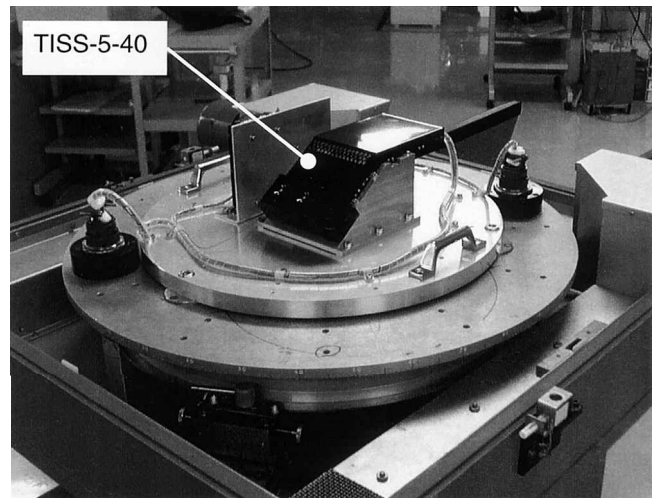


Figure 12. The single-axes rate table that was employed to evaluate for the accuracy of the scale factor.

The update of the quaternion at some time from t to $t + \Delta t$ is given in equation (15) by using a gyro output:

$$q(t + \Delta t) = q(t)X(t, \Delta t) \quad (15)$$

where $X(t, \Delta t)$ is a quaternion that represents the incremental attitude information obtained by the gyro loop. This sensor employs the third-order expansion, given in equation (16) for $X(t, \Delta t)$.

$$X(t, \Delta t) = 1 + \frac{\vec{\theta}}{2} - \frac{1}{2} \left(\frac{\vec{\theta}}{2} \cdot \frac{\vec{\theta}}{2} \right) - \frac{1}{6} \left(\frac{\vec{\theta}}{2} \cdot \frac{\vec{\theta}}{2} \right) \frac{\vec{\theta}}{2} - \frac{1}{6} \left(\frac{\vec{\theta}'}{2} \times \frac{\vec{\theta}}{2} \right) \quad (16)$$

Table 2. Results Compared with Specifications

Parameters		Specifications	Results
Heading accuracy		1 deg./hr. (1σ)	<1 deg./hr.
Attitude accuracy	Pitch	± 0.5 deg.	-0.06 deg. to +0.06 deg.
	Roll	± 0.5 deg.	-0.03 deg. to +0.04 deg.
Heading scale factor accuracy		$\pm 0.1\%$	-0.05% to +0.08%

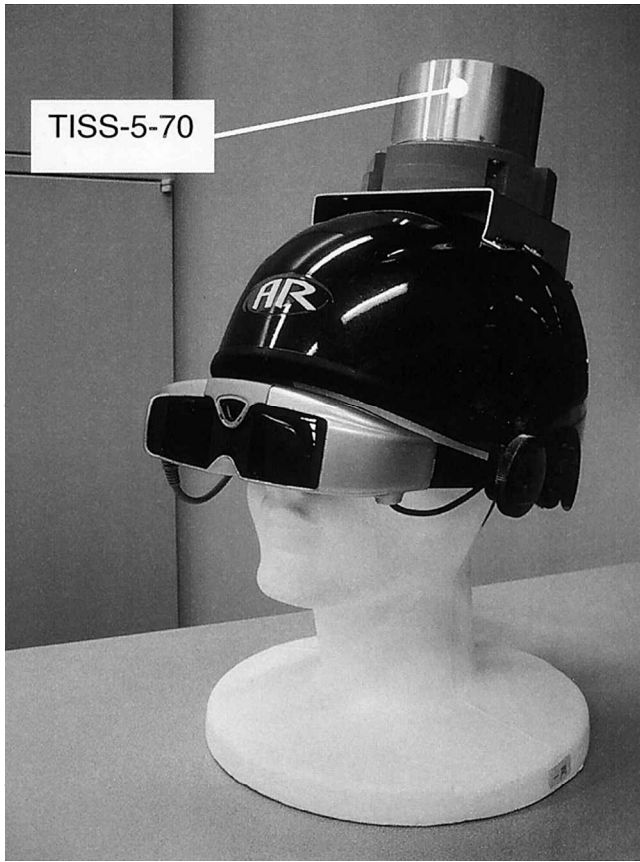


Figure 13. Outer view of prototype model as evaluated.

where

$$\frac{\ddot{\theta}}{2} = \frac{\ddot{\omega}\Delta t}{2} + \frac{\ddot{\omega}\Delta t^2}{4} + \frac{\ddot{\omega}\Delta t^3}{12} + \dots \quad (17)$$

$$\frac{\ddot{\theta}'}{2} = \left(-\ddot{\omega}\Delta t + \frac{\ddot{\omega}\Delta t^2}{2} - \frac{\ddot{\omega}\Delta t^3}{6} + \dots \right) \quad (18)$$

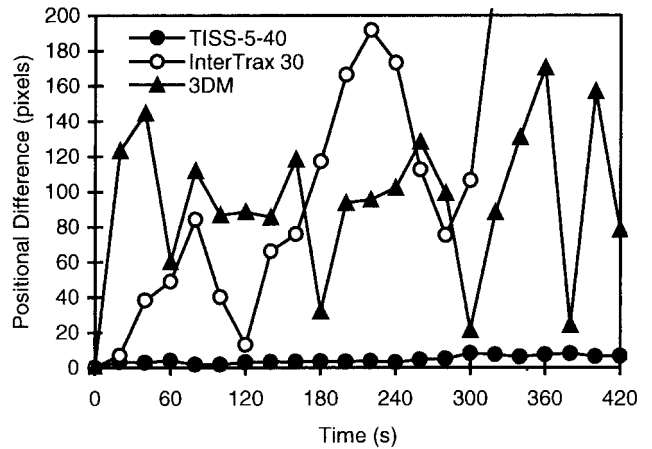


Figure 14. Comparison with other sensors.

and $\ddot{\omega}$ is the vector of rotation rate obtained from gyro output.

The outputs of the accelerometers on the body frame are transformed to the components of acceleration on the local frame and are divided by the earth's radius (R) and multiplied by proportional gain (K). This is fed back to the attitude-calculation section as compensatory rotation rates relative to the north axis and the east axis. The proportional gain (K) adjusts the effect of the feedback, and the value of proportional gain is obtained from the simulation about response of the sensor which considers a state of motion and an error quantity of the gyroscope and accelerometer. A filter is also set to minimize the accelerometer noise and not to influence the measurement of motion. Because of this feedback, it is possible to prevent any divergence in pitch and roll signals. However, heading stability depends on gyro bias stability because there is no feedback to restrict divergence in the heading calculation.

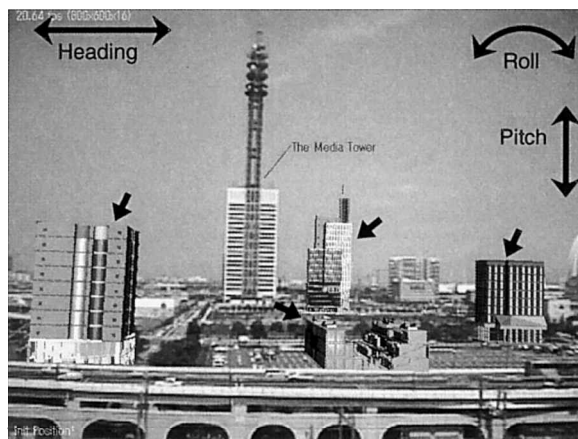


Figure 15. Overlaid image. The short arrows indicate the computer graphics images, and the long arrows indicate the three attitudes that correspond with the sensor output.

5 Evaluation of Performance

Sensor performance is evaluated based on TISS-5-40, and the results are shown in the following figures. Figure 8 shows heading drift. The heading drift was measured as the attitude of the sensor set, horizontally and north. Heading stability does not exceed 1 deg./hr. within 14 hr. from start. Figure 9 shows the accuracy of the attitude (pitch and roll), which was evaluated on the three-axes rate table (Contraves Goerz, model 53-3/30H, shown in figure 10 as a reference). The attitude does not exceed ± 0.1 deg. in the measurable range. Figure 11 shows the accuracy of scale factor. The scale factor was evaluated on the single-axis rate table (Contraves Goerz, model 61C/30H, shown in figure 12 as a reference). Accuracy of $\pm 0.1\%$ is achieved within the measured range. Table 2 shows a comparison between sensor specifications and evaluation results.

The results in applying the sensor in an actual mixed-reality system are as follows. These results were evaluated at the MR System Laboratory using prototype model TISS-5-70 (Hara et al., 2000). The outer view of the prototype model as evaluated is shown in figure 13. The sensor is fixed on a helmet with a head-mounted display and figure 14 shows the comparison with other sensors (such as the InterTrax 30 and the 3DM that was

performed at MR System Laboratory (Hara et al., 2000). In this experiment, the positional difference is defined as the average value of some distances on the screen between the specific image coordinate point and the real image coordinate point that corresponds to the point from a sensor output. The positional differences were measured at regular time intervals while the observer moved his head naturally in a helmet with the three fixed sensors. Positional differences using FOG are much smaller than the differences using the other sensors. Figure 15 shows an overlaid image obtained with this sensor. Sufficient image positioning is achieved with the absence of a sense of incongruity to the observer.

6 Conclusions

An attitude-measurement system has been developed utilizing FOG sensor technology that is finding increasing applications in airplanes, ships, and other mobile craft, and the system has demonstrated class performance of 1 deg./hr. An easy-to-use sensor system for wearable applications will be developed in the future with a focus on minimizing circuit size for compactness and light weight.

Acknowledgments

We are deeply thankful to Dr. Hiroyuki Yamamoto, Dr. Kiyohide Satoh, and all concerned at the MR system Laboratory for providing precious data for this paper.

References

- Azuma, R., Hoff, B., Neely, III, H., & Sarfaty, R. (1999). A motion stabilized outdoor augmented reality system. *Proceedings of VR99*, 252–259.
- Ezekiel, S., & Arditty, H. J. (1982). *Fiber-optic rotation sensors and related technologies*. Berlin: Springer-Verlag, 2–26.
- Foxlin, E., Harrington, M., & Pfeifer, G. (1998). Constellation: A wide-range wireless motion-tracking system for aug-

- mented reality and virtual set applications. *SIGGRAPH98 Conference Proceedings*, 371–378.
- Hara, K., Anabuki, M., Satoh, K., Yamamoto, H., & Tamura, H. (2000). A wearable mixed reality system for outdoor use: Design and implementation [in Japanese]. *Proceedings of VRSJ Annual Conference*, 407–410.
- Lefevre, H. (1993). *The fiber-optic gyroscope*. Norwood, MA: Artec House.
- Ohshima, T., Satoh, K., Yamamoto, H., & Tamura, H. (1999). RV-border guards: A multi-player mixed reality entertainment [in Japanese]. *TVRSJ*, 4(4), 699–705.
- McKern, Richard A. (1968). *A study of transformation algorithms for use in a digital computer*. Cambridge, MA: Massachusetts Institute of Technology, Dept of Aeronautics and Astronautics.
- Tamura, H., & Ohta, Y. (1998). Mixed reality [in Japanese]. *Journal of ITE*, 52(3), 266–272.
- Ulrich, R. (1980). Fiber-optic rotation sensing with low drift. *Optics Letters* 5, 173–175.